Applied Physics Letters

RESEARCH ARTICLE | AUGUST 04 2023

Strain effects on stability of topological ferroelectric polar configurations in $(PbTiO_3)_n/(SrTiO_3)_n$ superlattices

Cheng Dai ; Zijian Hong ; Sujit Das ; Yun-Long Tang ; Lane W. Martin ; Ramamoorthy Ramesh ; Long-Qing Chen

Appl. Phys. Lett. 123, 052903 (2023)
https://doi.org/10.1063/5.0160901
CHORUS

AIP Publishing

Applied Physics Letters ARTICLE pubs.aip.org/aip/apl

Strain effects on stability of topological ferroelectric polar configurations in $(PbTiO_3)_n/(SrTiO_3)_n$ superlattices

Cite as: Appl. Phys. Lett. **123**, 052903 (2023); doi: 10.1063/5.0160901
Submitted: 6 June 2023 · Accepted: 24 June 2023 ·
Published Online: 4 August 2023

Cheng Dai,[1,a)] Zijian Hong,[2] Sujit Das,[3] Yun-Long Tang,[4,5] Lane W. Martin,[4] Ramamoorthy Ramesh,[4] and Long-Qing Chen[1,a)]

AFFILIATIONS

[1]Department of Materials Science and Engineering and Materials Research Institute, The Pennsylvania State University, University Park, Pennsylvania 16802, USA
[2]Lab of Dielectric Materials, School of Materials Science and Engineering, Zhejiang University, Hangzhou 310027, China
[3]Materials Research Centre, Indian Institute of Science, Bangalore, Karnataka 560012, India
[4]Department of Materials Science and Engineering, University of California, Berkeley, California 94720, USA
[5]Shenyang National Laboratory for Materials Science Institute of Metal Research, Chinese Academy of Sciences, Shenyang 110016, China

[a)]**Authors to whom correspondence should be addressed:** daicheng1993313@gmail.com and lqc3@psu.edu

ABSTRACT

The $(PbTiO_3)_n/(SrTiO_3)_n$ (PTO/STO) superlattice system has been shown to exhibit interesting topological phases (e.g., vortices and skyrmions) in addition to normal ferroelectric domain states. Existing studies are mostly focused on the dependence of topological polar distributions and properties of PTO/STO superlattice on its periodicity. Here, we study the strain effect on the topological phase transitions and ferroelectric domain structures employing phase-field simulations. We summarized in an isotropic strain (in-plane misfit strain along the x direction is equal to that along the y direction) periodicity phase diagram displaying the stability regions of different polar topological states, including normal ferroelectric twins, vortices, skyrmions, and mixtures of vortices and twins. We also analyzed the polarization configurations under anisotropic in-plane strains (in-plane misfit strain along the x direction is not equal to that along the y direction) and demonstrated that the strain anisotropy can be used to tune the directions of vortex arrays along either the $[100]_{pc}$ or $[010]_{pc}$ directions or labyrinth vortex arrays. This work offers guidance to manipulating polar structures in the PTO/STO superlattices via strain engineering.

Recent studies have demonstrated the existence of rich nontrivial topological phases, including flux closures,[1] vortices,[2] polar skyrmions,[3] merons,[4] dipolar waves,[5] and anti-vortices in $(PbTiO3)_n/(SrTiO3)_n$ (PTO/STO) superlattices and $PbTiO_3$ thin films.[6–9] The dependence of polar structures on the superlattice periodicity for the PTO/STO superlattices on $DyScO_3$ (DSO) substrates was established by Hong *et al.*[10] They demonstrated that periodic arrays of vortex (the topological phase with rotational polarizations around an axis) tubes lying within the PTO planes form in superlattices with intermediate periodicity (>10 unit cells) while a-twin structure (the ferroelectric twin structure constructed with a_1 domain with polarization along the x direction and a_2 domain with polarization along the y direction) is stable at a small superlattice period (<10 unit cells). Furthermore, it has also been found that epitaxial misfit strains imposed by various substrates may lead to different mesoscale domain structures. For example, polar vortices evolve into skyrmions for the same PTO/STO superlattices when the substrate is changed from DSO to STO.[3] The anisotropy of strains may also be important as it was found in PTO.[11,12] Notably, strain here is specified as the effective lattice mismatch between PTO and substrate. The expression of the strain is shown in the supplementary material followed by previous studies.[13]

The main objective of this work is to study the strain effects on domain structures and topological phases and establish a phase diagram representing the stability of different polar phases under different strains. In particular, we constructed a strain–periodicity phase diagram and a misfit strain–misfit strain diagram for PTO/STO superlattices, which can provide guidance to the design of superlattice-based material systems and strain engineering of topological polar phases.

We employ phase-field method to obtain the three-dimensional polarization domain structures for the PTO/STO superlattice.[14–20] The evolution of spontaneous polarization is governed by the time-dependent Ginzburg–Landau (TDGL) equations,

$$\frac{\partial P_i(\vec{r},t)}{\partial t} = -L\frac{\delta F}{\delta P_i(\vec{r},t)} \quad (i = 1,2,3),$$

where L is the kinetics coefficient and t is the evolution time step. F is the total free energy of the heterostructure system,

$$F = \int (f_{landau} + f_{Elastic} + f_{Electric} + f_{Gradient})dV,$$

where f_{Landau} is the Landau free energy density as a function of spontaneous polarization, $f_{Elastic}$ is the elastic energy density as a function of mechanical displacements and spontaneous polarization, $f_{Electric}$ is the electrostatic energy density as a function of electric potential and spontaneous polarization, and $f_{Gradient}$ is the spontaneous polarization gradient energy. The elastic displacements are obtained by solving the mechanical equilibrium equation for a given spontaneous polarization and, thus, spontaneous strain under specified mechanical boundary conditions. At the same time, the electric potential is determined by solving the electrostatic Poisson equation for a given distribution of spontaneous polarization under the specific electric boundary conditions using a background dielectric constant for the heterostructure. All related simulation parameters are fully listed in Table S1 in the supplementary material.

The superlattice system chosen here is $(PbTiO_3)_n/(SrTiO_3)_n$ discretized with a mesh of $200 \times 200 \times 250$ grids, in which each grid represents 0.4 nm in real space. There are n unit cells of PTO and STO materials periodically repeated for five times. The pseudocubic lattice parameters of PTO and STO are 3.9574 and 3.905 Å, respectively.[16,21] We employ periodic boundary conditions along the in-plane directions and a superposition method along the out-of-plane direction. The electric potential is set as zero on the bottom and zero on the top of the superlattice film, which simulates the full compensation of film surface polarization charge by the top and bottom electrodes. A thin film mechanical boundary condition is employed, which is stress free at the film's top surface and fixes the elastic displacement in the substrate away from the substrate/film surface. More details for phase-field simulations have been reported in previous studies.[10,17,22]

Examples of typical domain structures and topological phases in PTO/STO superlattices from phase-field simulations are shown in Fig. 1. Figure 1(a) shows the typical c domains (ferroelectric domains with spontaneous polarization along both the $+z$ and $-z$ directions) with 180° mixed Ising–Néel type domain wall under a sufficiently large compressive strain ($\varepsilon_{xx} = \varepsilon_{yy} = -2\%$). Details of domain walls are shown in Fig. S1 in the supplementary material. For the case with a compressive strain, $\varepsilon_{xx} = \varepsilon_{yy} = -1.34\%$, the strain imposed by a STO substrate, shown in Fig. 1(b), a polar skyrmion (a topological structure consisting of $c-$ domains with negative polarization along the $-z$ direction is surrounded by $c+$ domains with positive polarization along the $+z$ direction or vice versa) is obtained. A full three-dimensional picture of a polar bubble skyrmion is obtained in Fig. S2 in the supplementary material. The result is consistent with that observed by Das *et al.* via scanning transmission electron microscopy (STEM) observations.[3] Under an intermediate strain ($\varepsilon_{xx} = \varepsilon_{yy} = -0.187\%$) and the lattice misfit strain on a DSO substrate (in-plane lattice constants along x and y directions for a DSO substrate are close and we simply consider the in-plane strain imposed by a DSO substrate isotropic),[23] vortices plotted in Fig. 1(c) are stable with a proper depolarization field strength. Under a large tensile strain, e.g., $\varepsilon_{xx} = \varepsilon_{yy} = 1.56\%$, a-twin states are stable [Fig. 1(d)]. One would be noticed that a sufficiently large volume (on the order of several millions of non-identical unit cells) for a superlattice system is needed to generate a proper polar domain pattern, which may be computationally very expensive. To reduce the computational cost, we do not perform simulations with pretty small (<8 unit cells) or large periodicities (>18 unit cells); thus, some polar structures induced by periodicities smaller than eight unit cells (wavy structure) and larger than 18 unit cells (flux closure) will not be discussed in this paper.

We performed a series of simulations with superlattice periodicity ranging from $n = 8$ to 18 unit cells under isotropic in-plane misfit strains (−2% to 0.317%). Based on the simulation results, we constructed a rather comprehensive domain stability diagram (Fig. 2). There are six polar structure regions, including two tetragonal states with out-of-plane polarizations (c domains) or in-plane polarizations along x and y directions (a_1/a_2 twin domains), two topological phases (skyrmion and vortex), and two regions consisting of a mixture of vortex and skyrmion (vortex + skyrmion) and a mixture of vortex and a_1/a_2 twin domains (vortex+ a_1/a_2). As shown in Fig. 2, the yellow region suggests that c domains are stable under large compressive strains. When the magnitude of the strain is reduced, or the superlattice periodicity is increased, the polar skyrmion phase (blue region, Fig. 2 is the most stable state. Upon further reducing the magnitude of

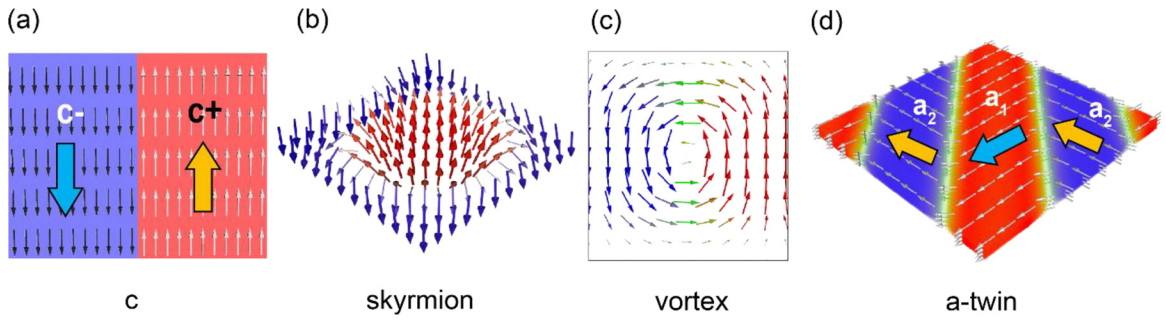

FIG. 1. Schematic of (a) $c-$ domains with 180° domain walls (details of domain walls are shown in Fig. S1 in the supplementary material); (b) schematic of a ferroelectric skyrmion; (c) schematic of a polar vortex with rotational polarization; and (d) schematic of the twin structure with a_1 and a_2 domains.

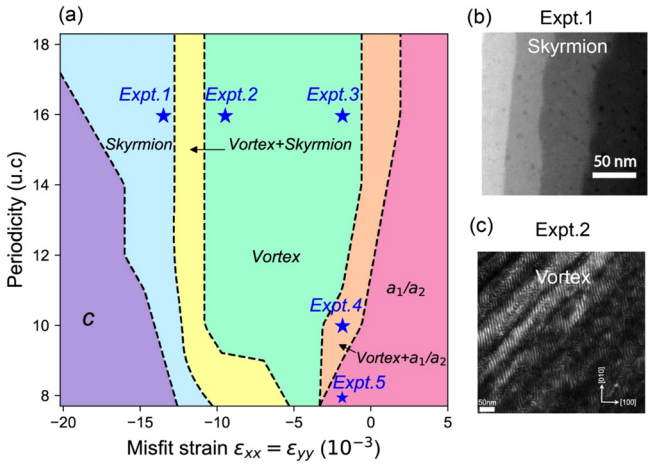

FIG. 2. The misfit strain effect on the PTO/STO superlattice system. (a) Misfit strain–periodicity phase diagram of the PTO/STO superlattice system. The caption inside the diagram indicates the stable domain structure for the colored region. Blue stars indicate experimental results. STEM images of the $(PTO)_{16}/(STO)_{16}$ superlattice on a (b) STO substrate and (c) SAGT substrate.

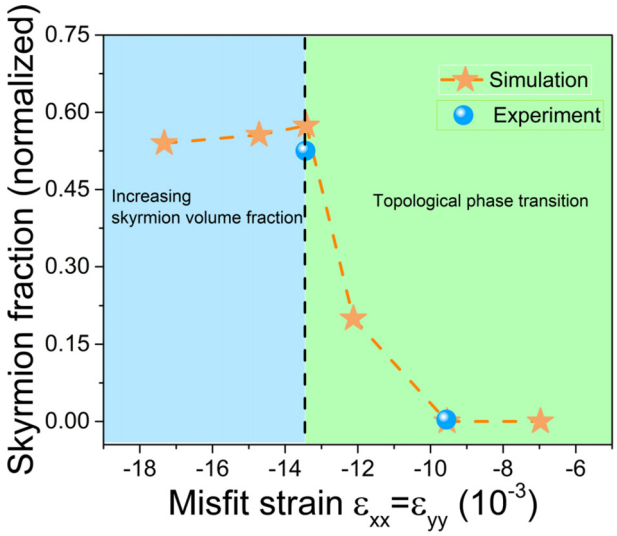

FIG. 3. Normalized skyrmion volume fraction with respect to isotropic misfit strain.

the compressive strain, vortex arrays form. Pure vortex arrays (purple area) exist under in-plane strains greater than −1% due to the increased in-plane polarization. Eventually, when the misfit strain becomes tensile (>0.187%), the *a*-twin structure (green area) becomes the most stable state. The strain–period phase diagram is likely influenced by differences in background dielectric constant, in-plane size, as well as initial polarization setup.

We analyzed the different forms of energy contributions to the stability of ferroelectric polar states shown in Fig. S3 in the supplementary material to understand the role of strain. The formation of *c* domains is dominated by the elastic energy reduction due to large compressive strains in both PTO and STO layers. With reduction in strain magnitude, the reduction in electric energy becomes increasingly dominant leading to the increase in the in-plane polarization and formation of skyrmions. When the strain is around −0.954%, the formation of vortices with rotational polarization reduces the gradient energy. Eventually, the formation of *a*-twin with in-plane polarization under a tensile strain is owing to the reduction in depolarization energy. In addition, at the boundaries between two stability regions, there exist two mixed states, vortex + skyrmion and vortex+a_1/a_2.

For validation, the experimental observations are included in Fig. 2(a) using blue stars. Two STEM images shown in Figs. 2(b) and 2(c) correspond to blue stars named Exp. 1 and 2 in Fig. 2(a), which represent topological structures (vortex and skyrmion) in the PTO/STO superlattice on STO (epitaxial misfit strain ∼ −1.34%) and $Sr_{1.04}Al_{0.12}Ga_{0.35}Ta_{0.50}O_3$ (SAGT, epitaxial misfit strain ∼ −0.954%) substrate, respectively. Meanwhile, blue stars named Exp. 3–5 in the diagram stand for experiments results from the previous literature.[10,24] The experimental observations largely confirm the simulation predictions. Sample preparation and STEM analysis details are shown in the supplementary material.

To analyze the transition from one polar structure to another, we plot the normalized skyrmion volume fraction in $(PTO)_{16}/(STO)_{16}$ superlattice vs anisotropic in-plane misfit strain diagram in Fig. 3.

Under a significantly compressive misfit strain (∼−1.78%), the calculated skyrmion volume fraction is around 51%. As the compressive strain decreases, the amount and magnitude of in-plane polarization increase, leading to the formation of a larger amount of skyrmions (Fig. S4 in the supplementary material). The skyrmion fraction grows to 57% at the misfit strain of −1.78%, which agrees well with previous experimental observation ∼52%.[8] Upon further decreasing the magnitude of the compressive strain to −1.34%, there is a topological phase transition from skyrmions to vortices (Fig. S5 in the supplementary material). Eventually, under a misfit strain ∼ −0.954% (corresponding

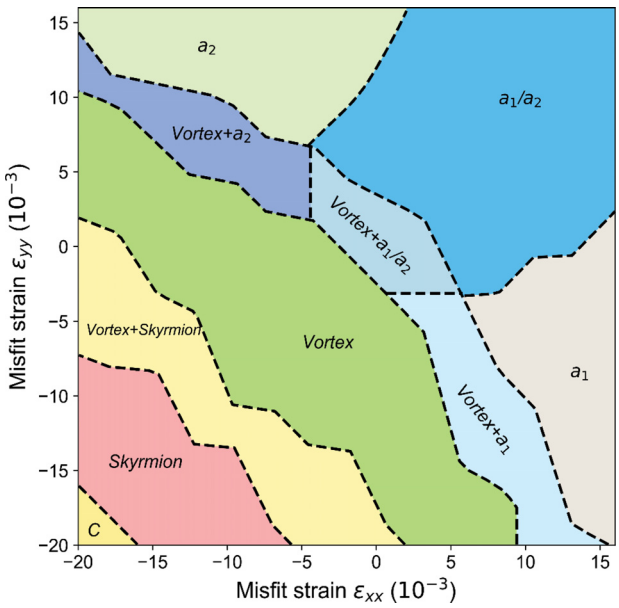

FIG. 4. Misfit strain (ε_{xx})–misfit strain (ε_{yy}) phase diagram for $(PTO)_{16}/(STO)_{16}$ superlattices at room temperature from phase-field simulations.

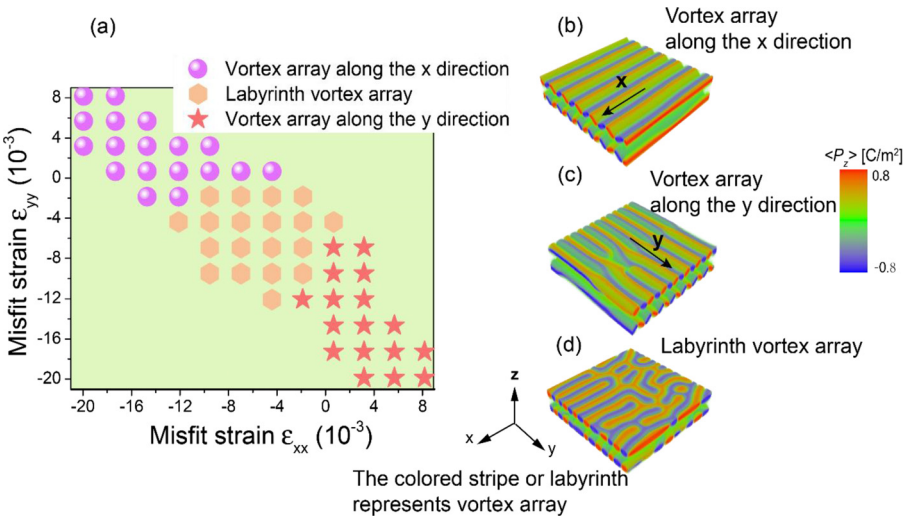

FIG. 5. (a) Misfit strain (ε_{xx})–misfit strain (ε_{yy}) vortex phase stability diagram: The purple dots represent vortex arrays along the *x* direction, orange hexagons represent labyrinth vortex arrays, and peach stars represent vortex arrays along the *y* direction. Examples of (b) vortex array along the *x* direction, (c) vortex array along the *y* direction, and (d) labyrinth vortex array.

to the SAGT substrate), no skyrmions are obtained, which is consistent with the STEM observation in Fig. 2(c). In-plane views of polar structural evolution with respect to the strain are provided in Fig. S5 in the supplementary material. The discussions above show that the skyrmion volume fraction evolves considerably under different misfit strains. Therefore, besides an external electric field,[8] skyrmion density and vortex-skyrmion topological phase transition could also be effectively tuned by strain.

We examined the effect of anisotropic strains on the relative stability of different polar states. In particular, we constructed a misfit strain–misfit strain phase diagram for the anisotropic strains in the range of $0.19\% < \varepsilon_{xx}$ and $\varepsilon_{yy} < 0.94\%$ for the PTO/STO superlattice system at room temperature with a specific superlattice period $n = 16$ unit cells. As shown in Fig. 4, ten different polarization states are observed, including *c*, a_1, a_2, a_1/a_2, vortex, skyrmion, vortex + skyrmion, mixed a_1 and vortex (vortex+ a_1), the mixed a_2 and vortex (vortex+ a_2), and vortex+ a_1/a_2. For those states mainly consisting of out-of-plane polarization such as *c*, skyrmion, vortex + skyrmion, and vortex regions, strains with this range of anisotropy only have a small impact on the polar phase stabilities. Due to respective tensile and compressive nature of the strains along the two in-plane directions, the average in-plane strain is small. Therefore, the anisotropic strain mainly affects the direction and magnitude of in-plane polarization and has negligible impact on out-of-plane polarization. As a result, strains with this range of anisotropy have little influence on the topological nature of skyrmions, which are *c*+ domains with polarization along the $+z$ direction surrounded by *c*- domains with polarization along the $-z$ direction. The topological charge is calculated by $\int\int \frac{1}{4\pi}\vec{P}\cdot(\partial_x\vec{P}\times\partial_y\vec{P})dxdy$, where $\vec{P}$ is the normalized polarization vector.[22,25,26] The value equaling to 1 represents the skyrmion topology as shown in Fig. S6 in the supplementary material. Under significantly large compressive strains ($>-2\%$ along one in-plane direction together with $<-1.6\%$ along with the other), *c* domains are stable. The polar skyrmion state is the stable state under smaller compressive strains ($-1.6\% < \varepsilon_{xx}$ and $\varepsilon_{yy} < -0.7\%$), while the vortex region is in the middle of the diagram plotted by salmon color. By contrast, the anisotropy of strains is the main factor of in determining either a_1, a_2, or a_1/a_2 twin structure as well as stabilities of vortex+a_1, vortex+a_2 and vortex+a_1/a_2 structures as the stable state (the top right region of the diagram). As expected, a tensile strain along the *x* or *y* direction favors the a_1 domains or a_2 domains.[12]

We observe three types of vortex arrays as a result of strain anisotropy giving rise to different in-plane polarization directions, including vortex arrays along the *x* (polar vortices with polarization rotated around the *x* axis) and *y* (polar vortices with polarization rotated around the *y* axis) directions as well as labyrinth arrays formed from mixtures of vortex arrays along both the *x* and *y* directions. As shown in Fig. 5, the vortex array is stable along the *x* or *y* direction under the more compressive strain along the *x* or *y* direction. Labyrinth vortex arrays tend to be stabilized by isotropic or close-to isotropic misfit strains. The cross section plots for all three types of arrays are shown in Fig. S7 in the supplementary material.

In summary, we established the strain–periodicity and the strain–strain phase diagrams of three-dimensional polar structures for PTO/STO superlattices employing the phase-field method. The phase diagram includes conventional ferroelectric domain structures and topological phases. The representative non-trivial topological phases (vortex, skyrmion) are tunable via the misfit strain. There are three types of vortex arrays, including vortex array along the *x* direction, along the *y* direction, and a different kind of labyrinth-vortex arrays. The work provides the guidance to employ strain to tune the polar structures of PTO/STO superlattices.

See the supplementary material for experimental and simulation details.

C.D., L.W.M., and L.-Q.C. acknowledge support the U.S. Department of Energy, Office of Science, Office of Basic Energy Sciences, under Award No. DE-SC-0012375 for the simulation and diffraction-based study of these materials. R.R. and S.D. acknowledges support from the Office of Basic Energy Sciences, U.S. Department of Energy (No. DE-AC02-05CH11231). L.W.M., R.R., and L.-Q.C. also acknowledge partial support of the Army Research Office under the ETHOS MURI via Cooperative

Agreement No. W911NF-21-2-0162. S. D. acknowledges the Science and Engineering Research Board (No. SRG/2022/000058) and the Indian Institute of Science start-up grant for financial support.

AUTHOR DECLARATIONS

Conflict of Interest

Long-Qing Chen is the owner of Mu-PRO LLC, which licensed the computer codes for generating the phase-field results from the Penn State Research Foundation. All other authors declare no conflicts of interest.

Author Contributions

Cheng Dai: Conceptualization (equal); Data curation (equal); Formal analysis (equal); Investigation (equal); Methodology (equal); Visualization (equal); Writing – original draft (equal); Writing – review & editing (equal). **Zijian Hong:** Conceptualization (equal); Methodology (equal); Writing – review & editing (equal). **Sujit Das:** Data curation (equal); Writing – review & editing (equal). **Yun-Long Tang:** Conceptualization (equal); Methodology (equal); Writing – review & editing (equal). **Lane W. Martin:** Formal analysis (equal); Resources (equal); Visualization (equal); Writing – original draft (equal). **Ramamoorthy Ramesh:** Conceptualization (equal); Data curation (equal); Formal analysis (equal); Investigation (equal); Methodology (equal); Resources (equal). **Long-Qing Chen:** Conceptualization (equal); Data curation (equal); Formal analysis (equal); Funding acquisition (lead); Investigation (equal); Methodology (equal); Project administration (equal); Resources (equal); Software (equal); Supervision (lead); Validation (equal); Visualization (equal); Writing – original draft (equal); Writing – review & editing (equal).

DATA AVAILABILITY

The data that support the findings of this study are available from the corresponding authors upon reasonable request. The phase-field simulation results in this work were obtained using the software package Mu-PRO (/www.mupro.com).

REFERENCES

[1]Y. L. Tang, Y. L. Zhu, X. L. Ma, A. Y. Borisevich, A. N. Morozovska, E. A. Eliseev, W. Y. Wang, Y. J. Wang, Y. B. Xu, Z. D. Zhang, and S. J. Pennycook, Science (80-) **348**, 547 (2015).
[2]A. K. Yadav, C. T. Nelson, S. L. Hsu, Z. Hong, J. D. Clarkson, C. M. Schlepütz, A. R. Damodaran, P. Shafer, E. Arenholz, L. R. Dedon, D. Chen, A. Vishwanath, A. M. Minor, L. Q. Chen, J. F. Scott, L. W. Martin, and R. Ramesh, Nature **530**, 198 (2016).
[3]S. Das, Y. L. Tang, Z. Hong, M. A. P. Gonçalves, M. R. McCarter, C. Klewe, K. X. Nguyen, F. Gómez-Ortiz, P. Shafer, E. Arenholz, V. A. Stoica, S. L. Hsu, B. Wang, C. Ophus, J. F. Liu, C. T. Nelson, S. Saremi, B. Prasad, A. B. Mei, D. G. Schlom, J. Íñiguez, P. García-Fernández, D. A. Muller, L. Q. Chen, J. Junquera, L. W. Martin, and R. Ramesh, Nature **568**, 368 (2019).
[4]Y. J. Wang, Y. P. Feng, Y. L. Zhu, Y. L. Tang, L. X. Yang, M. J. Zou, W. R. Geng, M. J. Han, X. W. Guo, B. Wu, and X. L. Ma, Nat. Mater. **22**, 636 (2023).
[5]F. H. Gong, Y. L. Tang, Y. L. Zhu, H. Zhang, Y. J. Wang, Y. T. Chen, Y. P. Feng, M. J. Zou, B. Wu, W. R. Geng, Y. Cao, and X. L. Ma, Sci. Adv. **7**, eabg5503 (2021).
[6]A. Y. Abid, Y. Sun, X. Hou, C. Tan, X. Zhong, R. Zhu, H. Chen, K. Qu, Y. Li, M. Wu, J. Zhang, J. Wang, K. Liu, X. Bai, D. Yu, X. Ouyang, J. Wang, J. Li, and P. Gao, Nat. Commun. **12**(1), 2054 (2021).
[7]L. Zhou, C. Dai, P. Meisenheimer, S. Das, Y. Wu, Y. Huang, J. Junquera, L.-Q. Chen, R. Ramesh, and Z. Hong, Adv. Funct. Mat. **1**, 211392 (2021).
[8]S. Das, Z. Hong, V. A. Stoica, M. A. P. Gonçalves, Y. T. Shao, E. Parsonnet, E. J. Marksz, S. Saremi, M. R. McCarter, A. Reynoso, C. J. Long, A. M. Hagerstrom, D. Meyers, V. Ravi, B. Prasad, H. Zhou, Z. Zhang, H. Wen, F. Gómez-Ortiz, P. García-Fernández, J. Bokor, J. Íñiguez, J. W. Freeland, N. D. Orloff, J. Junquera, L. Q. Chen, S. Salahuddin, D. A. Muller, L. W. Martin, and R. Ramesh, Nat. Mater. **20**, 194–201 (2020).
[9]E. Bousquet, M. Dawber, N. Stucki, C. Lichtensteiger, P. Hermet, S. Gariglio, J. M. Triscone, and P. Ghosez, Nature **452**, 732 (2008).
[10]Z. Hong, A. R. Damodaran, F. Xue, S. L. Hsu, J. Britson, A. K. Yadav, C. T. Nelson, J. J. Wang, J. F. Scott, L. W. Martin, R. Ramesh, and L. Q. Chen, Nano Lett. **17**, 2246 (2017).
[11]X. W. Guo, M. J. Zou, Y. J. Wang, Y. L. Tang, Y. L. Zhu, and X. L. Ma, Acta Mater. **206**, 116639 (2021).
[12]G. Sheng, J. X. Zhang, Y. L. Li, S. Choudhury, Q. X. Jia, Z. K. Liu, and L. Q. Chen, J. Appl. Phys. **104**, 2 (2008).
[13]F. Xue, J. J. Wang, G. Sheng, E. Huang, Y. Cao, H. H. Huang, P. Munroe, R. Mahjoub, Y. L. Li, V. Nagarajan, and L. Q. Chen, Acta Mater. **61**, 2909 (2013).
[14]J. J. Wang, X. Q. Ma, Q. Li, J. Britson, and L. Q. Chen, Acta Mater. **61**, 7591 (2013).
[15]Z. Hong, J. Britson, J. M. Hu, and L. Q. Chen, Acta Mater. **73**, 75 (2014).
[16]G. Sheng, Y. L. Li, J. X. Zhang, S. Choudhury, Q. X. Jia, V. Gopalan, D. G. Schlom, Z. K. Liu, and L. Q. Chen, Appl. Phys. Lett. **96**, 232902 (2010).
[17]Y. L. Li, S. Y. Hu, Z. K. Liu, and L. Q. Chen, Appl. Phys. Lett. **81**, 427 (2002).
[18]Y. L. Li, S. Y. Hu, Z. K. Liu, and L. Q. Chen, Acta Mater. **50**, 395 (2002).
[19]L. Q. Chen, Annu. Rev. Mater. Res. **32**, 113 (2002).
[20]L. Q. Chen and J. Shen, Comput. Phys. Commun. **108**, 147 (1998).
[21]M. J. Haun, E. Furman, S. J. Jang, H. A. McKinstry, and L. E. Cross, J. Appl. Phys. **62**, 3331 (1987).
[22]C. Dai, V. A. Stoica, S. Das, Z. Hong, L. W. Martin, R. Ramesh, J. W. Freeland, H. Wen, V. Gopalan, and L. Chen, Adv. Mater **34**, 2106401 (2022).
[23]M. Janovská, P. Sedlák, H. Seiner, M. Landa, P. Marton, P. Ondrejkovič, and J. Hlinka, J. Phys. Condens. Matter **24**, 385404 (2012).
[24]A. R. Damodaran, J. D. Clarkson, Z. Hong, H. Liu, A. K. Yadav, C. T. Nelson, S. L. Hsu, M. R. McCarter, K. D. Park, V. Kravtsov, A. Farhan, Y. Dong, Z. Cai, H. Zhou, P. Aguado-Puente, P. Garcia-Fernandez, J. Iniguez, J. Junquera, A. Scholl, M. B. Raschke, L. Q. Chen, D. D. Fong, R. Ramesh, and L. W. Martin, Nat. Mater. **16**, 1003 (2017).
[25]N. Nagaosa and Y. Tokura, Nat. Nanotechnol. **8**, 899 (2013).
[26]Z. Hong and L. Chen, Acta Materialia **152**, 155 (2018).